Computational Materials Science 124 (2016) 456–470

Contents lists available at ScienceDirect

Computational Materials Science

journal homepage: www.elsevier.com/locate/commatsci

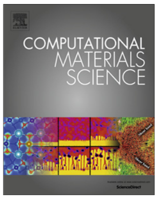

Numerical analysis of macrosegregation in vertically solidified Pb-Sn test castings – Part II: Equiaxed solidification

Y. Zheng [a], M. Wu [a,b,*], A. Kharicha [a,b], A. Ludwig [a]

[a] Chair of Modelling and Simulation of Metallurgical Processes, Montanuniversitaet Leoben, Austria
[b] Christian Doppler Laboratory for Advanced Simulation of Solidification and Melting, Montanuniversitaet Leoben, Austria

ARTICLE INFO

Article history:
Received 22 April 2016
Received in revised form 14 July 2016
Accepted 16 July 2016
Available online 5 August 2016

Keywords:
Macrosegregation
Equiaxed solidification
Nucleation
Crystal sedimentation
Equiaxed-to-columnar-transition (ECT)

ABSTRACT

In order to get basic understandings of the macrosegregation mechanisms, 8 test cases of a 2D casting ($50 \times 60\ \text{mm}^2$) with unidirectional cooling from either top or bottom were simulated. Part I of this two-part study has presented 4 cases of pure columnar solidification. Part II will present the other 4 cases of equiaxed solidification. Two alloys were considered: Sn–10 wt%Pb with solute element Pb heavier than the solvent Sn; Pb–18 wt%Sn with solute element Sn lighter than the solvent Pb. The solidified equiaxed crystal is considered always heavier than the melt. With such simple configurations, it is believed that the macrosegregation tendency during equiaxed solidification can be estimated. However, the modeling results show that complicated macrosegregation patterns can develop due to the complexity of the event of equiaxed-to-columnar transition (ECT). Analysis of the segregation mechanisms for each case is made. The three-phase mixed columnar-equiaxed solidification model (Wu and Ludwig, MMTA, 2006, p. 1613) is modified and used for this study. One modification is to consider the heterogeneous nucleation of equiaxed crystals and transport of inoculants (embryos). The inoculants serve as heterogeneous nucleation sites for the equiaxed crystals, which can be transported as well. Another modification is to include the ECT. When all inoculants are consumed and the equiaxed crystals settle down in the bottom region, the remaining melt in the upper part can only solidify as columnar structure. Those columnar structures develop/grow from the packed equiaxed crystals by triggering the event of ECT.

1. Introduction

1.1. Motivation

In order to provide exercise examples for metallurgical students to learn different macrosegregation mechanisms, a simple 2D casting with ideal configuration of pure columnar solidification or equiaxed solidification was designed and taught in the annual "solidification course" of EPFL held in Les Diablerets, Switzerland [1,2]. As shown in Fig. 1, 8 simple test cases were configured. They were unidirectionally cooled from either top or bottom. Two different alloys were considered: Sn-10 wt%Pb with solute element Pb heavier than the solvent Sn; Pb-18 wt%Sn with solute element Sn lighter than the solvent Pb. It is believed that, based on our theoretical knowledge and experience which we had previously, we should be able to estimate the global macrosegregation tendency without performing any numerical simulation. The current work is to simulate these 8 test cases by using a three-phase mixed columnar-equiaxed solidification model [3]. One purpose is to test the theoretical knowledge and experience. A more important purpose is to demonstrate the potential complexity of the macrosegregation phenomena. The current study is divided into two parts. In part I the 4 test cases of pure columnar solidification have been presented [4]. This paper, as Part II, will present other 4 test cases of equiaxed solidification, i.e. the scenarios as shown schematically in cases E1 through E4 of Fig. 1.

1.2. Challenge of modeling equiaxed solidification

Understanding to the equiaxed solidification was significantly improved in the last decades [5,6], but most important knowledge about the crystal transport, i.e. one origin of macrosegregation, is missing [7]. Although the importance of that transport phenomenon has been addressed for decades [8], there is no mature theory to describe the relationship between the crystal transport and the resulting structural heterogeneity and macrosegregation until some numerical models were developed recently [9,10].

---

[*] Corresponding author at: Chair of Modelling and Simulation of Metallurgical Processes, Montanuniversitaet Leoben, Austria.

E-mail address: menghuai.wu@unileoben.ac.at (M. Wu).

http://dx.doi.org/10.1016/j.commatsci.2016.07.018
0927-0256/

Nomenclature

c_0	initial concentration (1)
c_ℓ, c_e, c_c	species concentration (1)
c^{ref}	reference concentration (1)
c_{eu}	eutectic concentration (1)
$c^*_\ell,\ c^*_e,\ c^*_c$	equilibrium concentration at interface (1)
$C^p_{\ell e}$	species exchange between liquid and equiaxed ($kg\,m^{-3}\,s^{-1}$)
$C^p_{\ell c}$	species exchange between liquid and columnar ($kg\,m^{-3}\,s^{-1}$)
c^{index}	macrosegregation index (%)
c_{mix}	mix concentration (1)
$c^\ell_p,\ c^e_p,\ c^c_p$	specific heat ($J\,kg^{-1}\,K^{-1}$)
D_ℓ	diffusion coefficient ($m^2\,s^{-1}$)
d_e	equiaxed grain diameter (m)
d_c	columnar trunk diameter (m)
$f_\ell,\ f_e,\ f_c$	volume fraction of different phases (1)
f_{si}	dendrite to equiaxed volume ratio in the envelope (1)
f^{free}_c	critical f_c for free moving equiaxed phase (1)
f^{Env}_e	volume fraction of equiaxed grain envelope (1)
$f_{e,CET}$	critical equiaxed phase f_e under which the primary dendrite tip growth would be blocked (1)
$f_{e,packing}$	equiaxed grain packing limit (1)
$\vec{g}$	gravity ($m\,s^{-2}$)
$\vec{g}'_e,\ \vec{g}'_\ell$	reduced gravity ($m\,s^{-2}$)
h	heat transfer coefficient ($W\,m^{-2}\,K^{-1}$)
H^*	volume heat transfer coefficient between phases ($W\,m^{-3}\,K^{-1}$)
$h_\ell,\ h_e,\ h_c$	enthalpy ($J\,kg^{-1}$)
$h^{ref}_\ell,\ h^{ref}_e,\ h^{ref}_c$	reference enthalpy ($J\,kg^{-1}$)
Δh	latent heat ($J\,kg^{-1}$)
K	permeability of liquid in porous medium (m^2)
$K_{\ell e}(=-K_{e\ell})$	the drag force coefficient ($kg\,m^{-3}\,s^{-1}$)
k	solute partitioning coefficient at the liquid solid interface (1)
k_ℓ, k_e, k_c	thermal conductivity ($W\,m^{-1}\,K^{-1}$)
l	actual columnar length in tip cell (m)
$M_{\ell e}(=-M_{e\ell})$	liquid-equiaxed net mass transfer rate ($kg\,m^{-3}\,s^{-1}$)
$M_{\ell c}(=-M_{c\ell})$	liquid-columnar net mass transfer rate ($kg\,m^{-3}\,s^{-1}$)
m	slope of liquidus in phase diagram (K)
N_{nu}	equiaxed grain production rate by nucleation ($m^{-3}\,s^{-1}$)
n_{em}	inoculant number density (m^{-3})
n_{eq}	equiaxed grain number density (m^{-3})
n_c	columnar trunk number density (m^{-3})
n_{max}	maximum equiaxed grain volume density, or maximum available nucleation sites in simultaneous nucleation law (m^{-3})
p	pressure ($N\,m^{-2}$)
$Q_{\ell e}(=-Q_{e\ell})$	total energy exchange between liquid and equiaxed phases ($J\,m^{-3}\,s^{-1}$)
$Q^d_{\ell e}(=-Q^d_{e\ell})$	energy transfer between liquid and equiaxed phases ($J\,m^{-3}\,s^{-1}$)
$Q^p_{\ell e}(=-Q^p_{e\ell})$	energy exchange due to phase change between liquid and equiaxed phases ($J\,m^{-3}\,s^{-1}$)
$Q_{\ell c}(=-Q_{c\ell})$	total energy exchange between liquid and columnar phases ($J\,m^{-3}\,s^{-1}$)
$Q^d_{\ell c}(=-Q^d_{c\ell})$	energy transfer between liquid and columnar phases ($J\,m^{-3}\,s^{-1}$)
$Q^p_{\ell c}(=-Q^p_{c\ell})$	energy exchange due to phase change between liquid and columnar phases ($J\,m^{-3}\,s^{-1}$)
$Q_{ec}(=-Q_{ce})$	total energy exchange between equiaxed and columnar phases ($J\,m^{-3}\,s^{-1}$)
$Q^d_{ec}(=-Q^d_{ce})$	energy transfer between equiaxed and columnar phases ($J\,m^{-3}\,s^{-1}$)
$Q^p_{ec}(=-Q^p_{ce})$	energy exchange due to phase change between equiaxed and columnar phases ($J\,m^{-3}\,s^{-1}$)
R_{tip}	primary dendrite tip radius (m)
$R\ (R_e, R_c)$	grain radius (equiaxed, columnar) (m)
$R_{f,e}$	maximum radius of equiaxed grain (m)
$R_{f,c}$	maximum radius of columnar trunk (m)
T_0	initial temperature (K)
T, T_ℓ, T_e, T_c	temperature (K)
T_f	melting point of solvent at $c_0 = 0$ (K)
T_{ref}	reference temperature for enthalpy definition (K)
T_{eu}	eutectic temperature (K)
T_{liq}	liquidus temperature (K)
T_{EXT}	external temperature (K)
ΔT	constitutional undercooling (K)
ΔT_N	undercooling for maximum grain production rate (K)
ΔT_σ	Gaussian distribution width of nucleation law (K)
t	time (s)
Δt	time step (s)
$\vec{U}_{\ell e}(=-\vec{U}_{e\ell})$	total liquid-equiaxed momentum exchange rate ($kg\,m^{-2}\,s^{-2}$)
$\vec{U}^d_{\ell e}(=-\vec{U}^d_{e\ell})$	liquid-equiaxed momentum change due to drag force ($kg\,m^{-2}\,s^{-2}$)
$\vec{U}^p_{\ell e}(=-\vec{U}^p_{e\ell})$	liquid-equiaxed momentum exchange due to phase change ($kg\,m^{-2}\,s^{-2}$)
$\vec{U}_{\ell c}(=-\vec{U}_{c\ell})$	total liquid-columnar momentum exchange rate ($kg\,m^{-2}\,s^{-2}$)
$\vec{U}^d_{\ell c}(=-\vec{U}^d_{c\ell})$	liquid-columnar momentum change due to drag force ($kg\,m^{-2}\,s^{-2}$)
$\vec{U}^p_{\ell c}(=-\vec{U}^p_{c\ell})$	liquid-columnar momentum exchange due to phase change ($kg\,m^{-2}\,s^{-2}$)
$\vec{U}_{ce}$	total columnar-equiaxed momentum exchange rate ($kg\,m^{-2}\,s^{-2}$)
$\vec{U}^d_{ce}$	columnar-equiaxed momentum exchange rate due to drag ($kg\,m^{-2}\,s^{-2}$)
$\vec{U}^p_{ce}$	columnar-equiaxed momentum exchange rate due to phase change ($kg\,m^{-2}\,s^{-2}$)
$\vec{u}_\ell, \vec{u}_e, \vec{u}_c$	velocity vector ($m\,s^{-1}$)
$v_{Re},\ v_{Rc}$	grain growth speed in radius direction for equiaxed and columnar ($m\,s^{-1}$)
v_{tip}	grain growth speed in tip direction ($m\,s^{-1}$)
V_{domain}	volume of the calculated domain (m^3)
x, y	coordinate (m)
β_T	thermal expansion coefficient (K^{-1})
β_c	solutal expansion coefficient (1)
Γ	Gibbs Thomson coefficient (m K)
λ_1	primary columnar arm space (m)
μ_ℓ, μ_e	viscosity ($kg\,m^{-1}\,s^{-1}$)
$\rho_\ell,\ \rho_e,\ \rho_c$	density ($kg\,m^{-3}$)
ρ_{ref}	reference density ($kg\,m^{-3}$)
$\Delta\rho$	density difference between solid and liquid phase ($kg\,m^{-3}$)
ρ^b_ℓ	density for buoyancy force ($kg\,m^{-3}$)
$\bar{\bar{\tau}}_l,\ \bar{\bar{\tau}}_e$	stress-strain tensors ($kg\,m^{-1}\,s^{-1}$)

Subscripts

ℓ	mark liquid
e	equiaxed
c	columnar phases

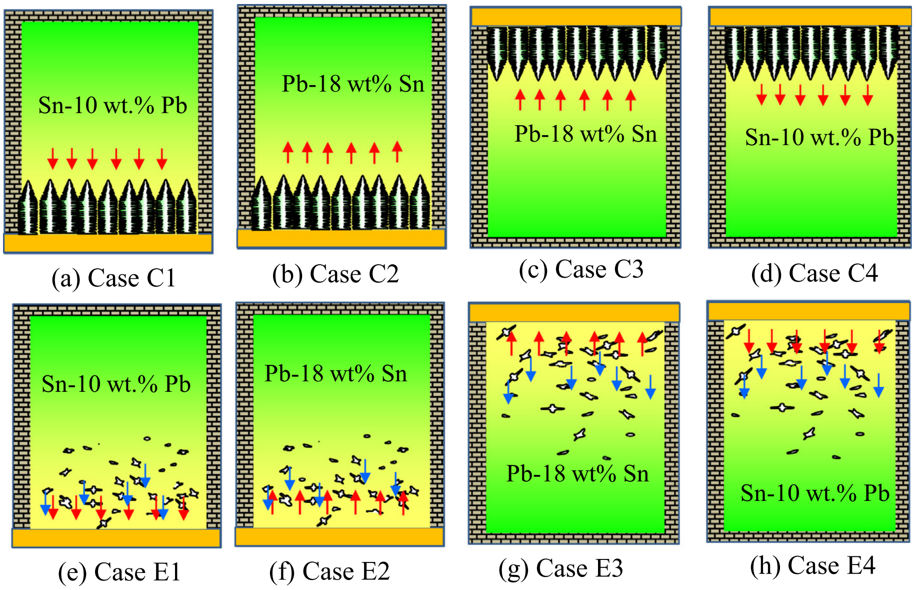

Fig. 1. Schematics of columnar (upper row) and equiaxed (lower row) solidification, solutal buoyancy force direction (red arrows) of the interdendritic/inter-granular melt, and crystal sedimentation direction (blue arrows) of the equiaxed grains. 8 cases were defined, where two different alloys were considered: Sn-10 wt%Pb with solute element Pb heavier than the solvent Sn; Pb-18 wt%Sn with solute element Sn lighter than the solvent Pb. The color gradients indicate the distribution of solute element in the melt: yellow for enrichment, green as the nominal composition. The yellow walls indicate chilled walls, while the hatched ones are adiabatic. Cases C1, C2, E1 and E2 were cooled from bottom, while the other 4 cases were cooled from top. (For interpretation of the references to color in this figure legend, the reader is referred to the web version of this article.)

A numerical model describing equiaxed solidification needs to consider nucleation, growth, sedimentation/flotation of equiaxed crystals, and melt flow. Therefore, a multiphase volume-average approach comes into favor [9,10]. The equiaxed crystals can be treated as a pseudo liquid phase (secondary fluid phase), interpenetrating and incorporating with the parent melt (primary fluid phase). The number density, grain size, moving velocity and other physical quantities of equiaxed crystals are volume-averaged and calculated by solving an additional set of conservation equations. Mass transfer due to solidification, momentum and energy transfer between the parent melt and the growing and moving equiaxed crystals are considered in closure laws. This approach was used by different authors to study the formation of macrosegregation during globular equiaxed solidification [11–14] and dendritic equiaxed solidification [15–19]. Recently, it was extended by Wu et al. for mixed columnar-equiaxed solidification, considering either non-dendritic [3,20–24] or dendritic growth of crystals [25–27]. To validate the numerical models, series of experiments based on various materials, e.g., NH_4Cl-H_2O [28,29], succinonitrile-acetone [30,31], Al-Cu alloy [32], and Sn-Pb alloy [33], were performed as well.

The volume-average based three-phase mixed columnar-equiaxed solidification model [3,34] with slight modifications is used in this paper. One modification is to consider the transport of inoculants (embryos). The inoculants serve as heterogeneous nucleation sites for the equiaxed crystals. Another modification is to include the equiaxed-to-columnar-transition (ECT). During equiaxed solidification, when all inoculants are consumed and the equiaxed crystals settle down in the bottom region, the remaining melt in the upper part can only solidify as columnar structure.

2. Numerical model and simulation settings

2.1. Model in brief

The three-phase mixed columnar-equiaxed solidification model was described previously [3,34]. Here, only a brief outline of the model assumptions is given. Conservation equations, source terms and exchange terms, and some auxiliary equations are summarized in Table 1.

(1) Three phases are the primary liquid melt, equiaxed and columnar phases. Their volume fractions are f_ℓ, f_e and f_c with $f_\ell + f_e + f_c = 1$. Both the liquid and equiaxed phases are moving phases, for which the corresponding Navier-Stokes equations are solved. The columnar phase is assumed to be rigid and stationary.
(2) Equiaxed crystals originate from heterogeneous nucleation [35]. The nucleation rate is a function of undercooling, $\Delta T = T_f + mc_\ell - T$. Transport of both inoculants (embryos) and equiaxed crystals is described in Section 2.3.
(3) The columnar structural growth is triggered by equiaxed-to-columnar transition (ECT), and it is described in Section 2.2.
(4) Simple crystal morphology is assumed for the diffusion-governed solidification kinetics: spheres for equiaxed grains and step-wise cylinders for columnar tree trunks. The solidification of both columnar trunk and equiaxed grain is governed by diffusion; the concentration difference $(c_\ell^* - c_\ell)$ is the driving force for the solidification. Back diffusion in solid is neglected $(D_c, D_e = 0)$.
(5) To deal with the hydrodynamic interaction between phases, a simplified dendritic morphology for the equiaxed phase is assumed, and the concept of "equiaxed grain envelope" is employed [36]. A dendritic equiaxed crystal is described by the equiaxed grain envelope, which includes the solid 'dendrite' and the inter-dendritic melt. The ratio of the volume of solid 'dendrite' to the volume of the equiaxed grain envelope is predefined: f_{si}. Therefore, the volume fraction of equiaxed grain envelopes (f_e^{Env}) is related to the volume fraction of the net solid phase of equiaxed crystals (f_e) by $f_e^{Env} = f_e/f_{si}$. In this study, f_{si} is set as a constant value (0.5).
(6) Volume-averaged concentrations $(c_\ell,\ c_e,\ c_c)$ are calculated by Eqs. (6)–(8). Thermodynamic equilibrium is assumed at the liquid-solid interface, which dictates the concentrations

Table 1
Conservation equations, sources and exchange terms, and auxiliary equations.

1. Conservation equations		
Mass:	$\frac{\partial}{\partial t}(f_\ell\rho_\ell)+\nabla\cdot(f_\ell\rho_\ell\vec{u}_\ell)=M_{\mathrm{e}\ell}+M_{\mathrm{c}\ell}$	(1)
	$\frac{\partial}{\partial t}(f_\mathrm{e}\rho_\mathrm{e})+\nabla\cdot(f_\mathrm{e}\rho_\mathrm{e}\vec{u}_\mathrm{e})=M_{\ell\mathrm{e}}$	(2)
	$\frac{\partial}{\partial t}(f_\mathrm{c}\rho_\mathrm{c})=M_{\ell\mathrm{c}}$	(3)
Momentum:	$\frac{\partial}{\partial t}(f_\ell\rho_\ell\vec{u}_\ell)+\nabla\cdot(f_\ell\rho_\ell\vec{u}_\ell\otimes\vec{u}_\ell)=-f_\ell\nabla p+\nabla\cdot\bar{\bar{\tau}}_\ell+f_\ell\rho_\ell\vec{g}'_\ell-\vec{U}_{\ell\mathrm{e}}-\vec{U}_{\ell\mathrm{c}}$ with $\vec{g}'_\ell=\frac{\rho^\mathrm{b}_\ell(T,c)-\rho_\ell}{\rho_\ell}\vec{g}$, $\rho^\mathrm{b}_\ell(T,c)=\rho_\ell\cdot\left[1+\beta_\mathrm{T}\cdot(T^\mathrm{ref}-T_\ell)+\beta_\mathrm{c}\cdot(c^\mathrm{ref}-c_\ell)\right]$, $\vec{U}_{\ell\mathrm{e}}=\vec{U}^\mathrm{p}_{\ell\mathrm{e}}+\vec{U}^\mathrm{d}_{\ell\mathrm{e}}$, $\vec{U}_{\ell\mathrm{c}}=\vec{U}^\mathrm{p}_{\ell\mathrm{c}}+\vec{U}^\mathrm{d}_{\ell\mathrm{c}}$	(4)
	$\frac{\partial}{\partial t}(f_\mathrm{e}\rho_\mathrm{e}\vec{u}_\mathrm{e})+\nabla\cdot(f_\mathrm{e}\rho_\mathrm{e}\vec{u}_\mathrm{e}\otimes\vec{u}_\mathrm{e})=-f_\mathrm{e}\nabla p+\nabla\cdot\bar{\bar{\tau}}_\mathrm{e}+f_\mathrm{e}\rho_\mathrm{e}\vec{g}'_\mathrm{e}+\vec{U}_{\ell\mathrm{e}}+\vec{U}_\mathrm{ce}$	(5)
	with $\vec{g}'_\mathrm{e}=\frac{\Delta\rho}{\rho_\mathrm{e}}\vec{g}$, $\vec{U}_\mathrm{ce}=\vec{U}^\mathrm{p}_\mathrm{ce}+\vec{U}^\mathrm{d}_\mathrm{ce}$, $\Delta\rho=\rho_\mathrm{e}-\rho_\ell$.	
Species:	$\frac{\partial}{\partial t}(f_\ell\rho_\ell c_\ell)+\nabla\cdot(f_\ell\rho_\ell\vec{u}_\ell c_\ell)=\nabla\cdot(f_\ell\rho_\ell D_\ell\nabla c_\ell)-C^\mathrm{p}_{\ell\mathrm{c}}-C^\mathrm{p}_{\ell\mathrm{e}}$	(6)
	$\frac{\partial}{\partial t}(f_\mathrm{e}\rho_\mathrm{e}c_\mathrm{e})+\nabla\cdot(f_\mathrm{e}\rho_\mathrm{e}\vec{u}_\mathrm{e}c_\mathrm{e})=\nabla\cdot(f_\mathrm{e}\rho_\mathrm{e}D_\mathrm{e}\nabla c_\mathrm{e})+C^\mathrm{p}_{\ell\mathrm{e}}$	(7)
	$\frac{\partial}{\partial t}(f_\mathrm{c}\rho_\mathrm{c}c_\mathrm{c})=\nabla\cdot(f_\mathrm{c}\rho_\mathrm{c}D_\mathrm{c}\nabla c_\mathrm{c})+C^\mathrm{p}_{\ell\mathrm{c}}$	(8)
Enthalpy:	$\frac{\partial}{\partial t}(f_\ell\rho_\ell h_\ell)+\nabla\cdot(f_\ell\rho_\ell\vec{u}_\ell h_\ell)=\nabla\cdot(f_\ell k_\ell\nabla\cdot T_\ell)-Q_{\ell\mathrm{c}}-Q_{\ell\mathrm{e}}$	(9)
	$\frac{\partial}{\partial t}(f_\mathrm{e}\rho_\mathrm{e}h_\mathrm{e})+\nabla\cdot(f_\mathrm{e}\rho_\mathrm{e}\vec{u}_\mathrm{e}h_\mathrm{e})=\nabla\cdot(f_\mathrm{e}k_\mathrm{e}\nabla\cdot T_\mathrm{e})+Q_{\ell\mathrm{e}}+Q_\mathrm{ce}$ with $Q_{\ell\mathrm{e}}=Q^\mathrm{p}_{\ell\mathrm{e}}+Q^\mathrm{d}_{\ell\mathrm{e}}$, $Q_\mathrm{ce}=Q^\mathrm{p}_\mathrm{ce}+Q^\mathrm{d}_\mathrm{ce}$, $Q^\mathrm{d}_\mathrm{ce}=0$	(10)
	$\frac{\partial}{\partial t}(f_\mathrm{c}\rho_\mathrm{c}h_\mathrm{c})=\nabla\cdot(f_\mathrm{c}k_\mathrm{c}\nabla\cdot T_\mathrm{c})+Q_{\ell\mathrm{c}}-Q_\mathrm{ce}$ with $Q_{\ell\mathrm{c}}=Q^\mathrm{p}_{\ell\mathrm{c}}+Q^\mathrm{d}_{\ell\mathrm{c}}$, $h_\ell=\int_{T_\mathrm{ref}}^{T_\ell}c^\ell_\mathrm{p}dT+h^\mathrm{ref}_\ell$, $h_\mathrm{e}=h_c=\int_{T_\mathrm{ref}}^{T_\mathrm{e}}c^\mathrm{e}_\mathrm{p}dT+h^\mathrm{ref}_\mathrm{e}$, $L=h^\mathrm{ref}_\ell-h^\mathrm{ref}_\mathrm{e}$	(11)

2. Nucleation and transport of the equiaxed grains				
Trans. equation:	$\frac{\partial}{\partial t}n_\mathrm{em}+\nabla\cdot(\vec{u}_\ell n_\mathrm{em})=-N_\mathrm{nu}$	(12)	$\frac{\partial}{\partial t}n_\mathrm{eq}+\nabla\cdot(\vec{u}_\mathrm{e}n_\mathrm{eq})=N_\mathrm{nu}$	(13)
Nucleation:	$N_\mathrm{nu}=\frac{n_\mathrm{em}}{n_\mathrm{max}}\cdot\frac{D(\Delta T)}{Dt}\cdot\frac{dn}{d(\Delta T)}$	$\frac{D(\Delta T)}{Dt}=\frac{\partial T}{\partial t}+u_\ell\cdot(m\cdot\frac{\partial c_\ell}{\partial x}-\frac{\partial T_\ell}{\partial x})+v_\ell\cdot(m\cdot\frac{\partial c_\ell}{\partial y}-\frac{\partial T_\ell}{\partial y})$	$\frac{dn}{d(\Delta T)}=\frac{n_\mathrm{max}}{\sqrt{2\pi}\cdot\Delta T_\sigma}\cdot e^{-\frac{1}{2}\cdot\left(\frac{\Delta T-\Delta T_\mathrm{N}}{\Delta T_\sigma}\right)^2}$	(14)

3. Mass transfer					
Equiaxed			**Columnar**		
Equi. grain growth velocity:	$v_{R_\mathrm{e}}=\frac{dR_\mathrm{e}}{dt}=\frac{D_\ell}{R_\mathrm{e}(1-R_\mathrm{e}/R_\mathrm{f,e})}\cdot\frac{c^*_\ell-c_\ell}{c^*_\ell-c^*_\mathrm{e}}$	(15)	Col. trunk growth velocity:	$v_{R_\mathrm{c}}=\frac{dR_\mathrm{c}}{dt}=\frac{D_\ell}{R_\mathrm{c}}\cdot\frac{(c^*_\ell-c_\ell)}{(c^*_\ell-c^*_\mathrm{c})}\cdot\ln^{-1}\left(\frac{R_\mathrm{f,c}}{R_\mathrm{c}}\right)$	(16)
Mass transfer:	$M_{\ell\mathrm{e}}=v_{R_\mathrm{e}}\cdot(n_\mathrm{eq}\cdot\pi d^2_\mathrm{e})\cdot\rho_\mathrm{e}\cdot f_\ell$	(17)	Mass transfer for the trunks:	$M_{\ell\mathrm{c}}=v_{R_\mathrm{c}}\cdot(\pi d_\mathrm{c}/\lambda^2_1)\cdot\rho_\mathrm{c}\cdot\Phi_\mathrm{imp}$	(18)
			Mass transfer incl. col. tips:	$M_{\ell\mathrm{c}}=v_{R_\mathrm{c}}\cdot n_\mathrm{c}\cdot(\pi d_\mathrm{c}\cdot l)\cdot\rho_\ell\cdot\Phi_\mathrm{imp}+v_\mathrm{tip}\cdot n_\mathrm{c}\cdot(\pi R^2_\mathrm{tip})\cdot\rho_\ell\cdot\Phi_\mathrm{imp}$ with $\Phi_\mathrm{imp}=\begin{cases}1 & d_\mathrm{c}\le\lambda_1\\ 4f_\ell/(4-\pi) & d_\mathrm{c}>\lambda_1\end{cases}$	(19)

4. Source and exchange terms				
Momentum transfer:	$\vec{U}^\mathrm{p}_{\ell\mathrm{e}}=\vec{u}_\ell\cdot M_{\ell\mathrm{e}}$, $\vec{U}^\mathrm{p}_{\ell\mathrm{c}}=\vec{u}_\ell\cdot M_{\ell\mathrm{c}}$, $\vec{U}^\mathrm{p}_\mathrm{ce}=0$.	(20)	$\vec{U}^\mathrm{d}_{\ell\mathrm{e}}=K_{\ell\mathrm{e}}\cdot(\vec{u}_\ell-\vec{u}_\mathrm{e})$, $\vec{U}^\mathrm{d}_{\ell\mathrm{c}}=\frac{f^2_\ell\cdot\mu_\ell}{K}\cdot\vec{u}_\ell$ $\vec{U}^\mathrm{d}_\mathrm{ce}$ refers to [3], $K=6\times10^{-4}\cdot\lambda^2_1\cdot\frac{f^3_\ell}{(1-f_\ell)^2}$	(21)
Species transfer:	$C^p_{\ell\mathrm{e}}=k\cdot c^*_\ell\cdot M_{\ell\mathrm{e}}$, $C^\mathrm{p}_{\ell\mathrm{c}}=k\cdot c^*_\ell\cdot M_{\ell\mathrm{c}}$	(22)		
Enthalpy transfer and latent heat:	$Q^\mathrm{p}_{\ell\mathrm{e}}=h_\ell\cdot M_{\ell\mathrm{e}}$, $Q^\mathrm{p}_{\ell\mathrm{c}}=h_\ell\cdot M_{\ell\mathrm{c}}$	(23)	$Q^\mathrm{d}_{\ell\mathrm{e}}=H^*\cdot(T_\ell-T_\mathrm{e})$, $Q^\mathrm{d}_{\ell\mathrm{c}}=H^*\cdot(T_\ell-T_\mathrm{c})$, $Q^\mathrm{d}_\mathrm{ce}=H^*\cdot(T_\mathrm{c}-T_\mathrm{e})$, where $\mathrm{H}^*=10^9$ W·m^{-2}·K^{-1}	(24)

5. Auxiliary equations					
Mixture concentration $c_\mathrm{mix}=\frac{c_\ell\cdot\rho_\ell\cdot f_\ell+c_\mathrm{e}\cdot\rho_\mathrm{e}\cdot f_\mathrm{e}+c_\mathrm{c}\cdot\rho_\mathrm{c}\cdot f_\mathrm{c}}{\rho_\ell\cdot f_\ell+\rho_\mathrm{e}\cdot f_\mathrm{e}+\rho_\mathrm{c}\cdot f_\mathrm{c}}$	(25)	Macrosegregation index in % $c^\mathrm{index}=\frac{c_\mathrm{mix}-c_0}{c_0}\times100$	(26)	Global macrosegregation intensity $\mathrm{GMI}=\frac{1}{\mathrm{V_{domain}}}\cdot\iiint_{\mathrm{V_{domain}}}\lvert c^\mathrm{index}\rvert dV$	(27)

at the interface (c_ℓ^*, c_e^*, c_c^*). A linearized Pb-Sn binary phase diagram is used, and a constant solute redistribution coefficient k and a constant liquidus slope m are assumed.

(7) The macrosegregation is usually evaluated by the mixture concentration c_{mix}, as defined by Eq. (25), but here two additional quantities are defined to quantify the macrosegregation: one is the macrosegregation index c^{index}, Eq. (26), and another one is the global macrosegregation intensity (GMI), Eq. (27). The quantities of them are presented in %.

(8) Resistance of the mushy zone (columnar phase) to interdendritic flow is calculated using a permeability law according to Blake-Kozeny [37]. The drag force coefficient $K_{\ell e}$ for the melt-equiaxed interaction is treated according to Kozeny-Carman for $f_e < 0.7$, and Blake-Kozeny for $f_e \geqslant 0.7$ [37].

(9) The presence of equiaxed crystals influences the growth of primary dendrite tips. The critical volume fraction of equiaxed envelopes ($f_{e,\mathrm{CET}}$) to block the growth of the primary columnar dendrite tips is set as 0.49 [37]. When f_e^{Env} $(=f_e/f_{si})$ reaches $f_{e,\mathrm{CET}}$ at the columnar tip front, the columnar-to-equiaxed transition (CET) occurs.

(10) The presence of the columnar structure influences the motion of equiaxed crystals. The equiaxed crystals can be captured by the columnar dendrite trunk when the local volume fraction of the columnar phase reaches a critical value of $f_c^{\mathrm{free}} = 0.2$.

(11) The interactions between neighboring equiaxed crystals and their influence on the motion of equiaxed phase is modeled by a so-called effective viscosity (μ_e) [38], which increases with the volume fraction of the equiaxed phase. When the volume fraction of the grain envelope of equiaxed phase f_e^{Env} $(=f_e/f_{si})$ reaches the packing limit $f_{e,\mathrm{packing}}$, μ_e increases to infinitive, and a rigid network of equiaxed crystals is built. Here $f_{e,\mathrm{packing}}$ is equal to 0.637.

2.2. Equiaxed-to-columnar transition (ECT) and columnar-to-equiaxed transition (CET)

The terms equiaxed-to-columnar transition (ECT) and columnar-to-equiaxed transition (CET) have been used to describe the crystal structural transition between equiaxed and columnar during solidification of an alloy casting. After nucleation of crystals in undercooled melt, e.g., near the casting surface, growth of the crystals is generally equiaxed. With the progress of solidification, when a temperature gradient is gradually established, the growth of the crystals becomes unidirectionally against the heat flux direction. Columnar structure develops. This crystal structural transition from equiaxed to columnar is called as ECT. During the late stage of solidification, when new equiaxed crystals nucleate and grow in the liquid ahead of columnar zone, the growth of columnar structure will be blocked by the equiaxed crystals and the transition from columnar to equiaxed, i.e. CET, occurs. When the motion of equiaxed crystals and mechanical interaction between the dendritic crystals occur, the aforementioned ECT and CET become much more complex. They might not be simply explained by cooling direction (unidirectional or homogenous cooling). In order to treat the ECT and CET considering the crystal transport and interaction phenomena, following modeling concept is suggested.

During equiaxed solidification, equiaxed crystals can coagulate with each other. When the local volume fraction of equiaxed envelope $\left(f_e^{\mathrm{Env}} = f_e/f_{si}\right)$ becomes larger than a critical volume fraction ($f_{e,\mathrm{packing}}$), the equiaxed phase builds a rigid network. Here $f_{e,\mathrm{packing}}$ is called as packing limit, taking 0.637. As the equiaxed phase is arrested by the mold wall (stationary), the velocity of the equiaxed phase vanishes, and then the equiaxed phase is considered as rigid and stationary. Numerically, this rigid and stationary equiaxed phase region is marked. Columnar primary dendrite tips are allowed to initiate and grow from the outer contour of the marked region. The growth of the columnar primary dendrite tips is tracked explicitly. The numerical algorithm, as described previously to track the columnar tip front [34], is applied here. The growth velocity of the columnar primary dendrite tip is modeled according to LGK [39].

The solidification of the columnar phase region competes with the solidification of the equiaxed phase region. When the solidification of the columnar phase "overtakes" the solidification of equiaxed phase, the event of equiaxed-to-columnar transition (ECT) is triggered. Otherwise, the solidification of the columnar phase is suppressed, or the solidification of existing columnar primary tip front is blocked by equiaxed phase, i.e. columnar-to-equiaxed transition (CET) is triggered. In order to judge if the solidification of columnar phase can "overtake" the solidification of equiaxed phase, following algorithm is implemented. If the columnar primary dendrite tip front can grow out of the considered volume element before f_e^{Env} reaches a so-called blocking limit ($f_{e,\mathrm{CET}}$), the growth of columnar primary tip front can continue into the neighboring cell or cells. In opposite, if the columnar primary dendrite tip front cannot grow out of the considered volume element before f_e^{Env} reaches $f_{e,\mathrm{CET}}$, CET occurs. $f_{e,\mathrm{CET}}$ was suggested by Hunt to be 0.49 [37], but was recently modified to be 0.2 [38]. During the late stage of equiaxed solidification, the inoculants are consumed, i.e. no new equiaxed grain can nucleate, ECT event occurs and the rest domain of the casting solidifies as columnar structure. Therefore, the final ECT position is marked by the isoline of $f_e^{\mathrm{Env}} = f_{e,\mathrm{CET}}$.

2.3. Heterogeneous nucleation and transport of inoculants and equiaxed crystals

Heterogeneous nucleation law is verified for most technical alloys. Inoculants, i.e. nucleation embryos, exist in the parent melt. The inoculants will be activated by undercooling. The activated inoculants develop as equiaxed nuclei and they can grow. The undercooling needed to activate an inoculant depends on the size of the inoculant [40]. Empirically, it was found that the nucleation event follows a Gaussian distribution function of undercooling [35], as described by Eq. (14), and it is widely used in different solidification models.

The inoculants and equiaxed crystals are quantified by their number densities: n_{em} and n_{eq}. The transport of inoculants n_{em} is calculated by Eq. (12) according to liquid melt velocity $\vec{u}_\ell$, while the transport of equiaxed crystals n_{eq} is calculated by Eq. (13) according to the velocity of equiaxed phase $\vec{u}_e$. The source term N_{nu} determines the nucleation rate. The total number (volume integral) of inoculants and equiaxed crystals in the whole casting must be conserved: a certain number of inoculants consumed are identical to the number of newly-nucleated equiaxed crystals. Actually, the above idea is quite similar to that of Bedel et al. [41]. Please notice that different size groups of inoculants were treated by Bedel, and transport of each size group has to be calculated individually. In the current model, however, no size groups are distinguished. Only one transport equation for n_{em} is necessarily solved. Statistically, nucleation rate is estimated to be proportional to the local number density of inoculants (n_{em}).

2.4. Configuration of the test casting

The configuration of the 2D test casting is shown in Fig. 2. The geometry, alloys and most of material properties are taken from

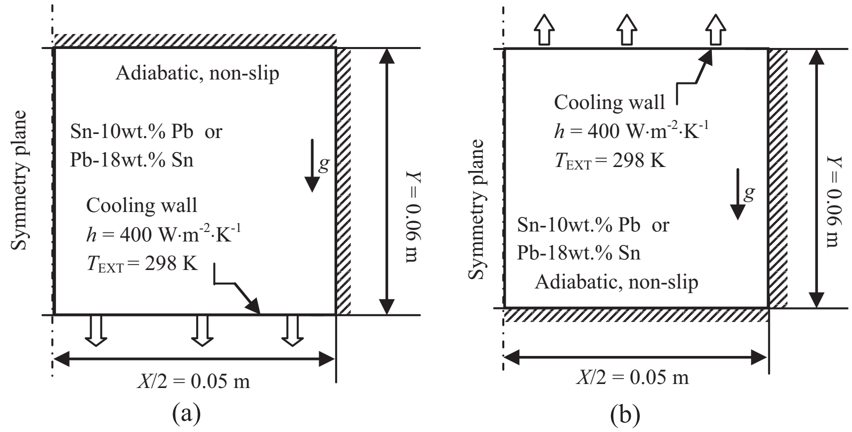

Fig. 2. Geometry of test cases with boundary and initial conditions.

Table 2
Material properties and other parameters.

	Symbol	Units	Sn-10 wt%Pb	Pb-18 wt%Sn	Ref.
Nominal concentration	c_0	–	10.0 wt%Pb	18.0 wt%Sn	
Liquidus temperature	T_{liq}	K	492.14	558.63	[42]
Melting point of solvent at $c_0 = 0$	T_{f}	K	505	600.65	[42]
Eutectic composition	c_{eu}	wt%	38.1	61.9	[42]
Eutectic temperature	T_{eu}	K	456	456	[35]
Liquidus slope	m	K (wt%)$^{-1}$	-1.286	-2.334	[42]
Equilibrium partition coefficient	k	–	0.0656	0.310	[42]
Reference density	ρ_{ref}	kg m^{-3}	7000	9250	[42]
Specific heat	$c_{\mathrm{p}}^{\ell},\ c_{\mathrm{p}}^{\mathrm{e}},\ c_{\mathrm{p}}^{\mathrm{c}}$	J kg^{-1} K^{-1}	260	176	[42]
Thermal conductivity	$k_{\ell},\ k_{\mathrm{e}},\ k_{\mathrm{c}}$	W m^{-1} K^{-1}	55.0	17.9	[42]
Latent heat	Δh_{f}	J kg^{-1}	6.1×10^{4}	3.76×10^{4}	[42]
Viscosity	μ_{ℓ}	kg m^{-1} s^{-1}	1.0×10^{-3}	1.1×10^{-3}	[42]
Liquid thermal expansion coefficient	β_{T}	K^{-1}	6.0×10^{-5}	1.16×10^{-4}	[42]
Liquid solutal expansion coefficient	β_{C}	wt%$^{-1}$	-5.3×10^{-3}	4.9×10^{-3}	[42]
Primary dendritic arm spacing	λ_1	m	1.3×10^{-3}	1.85×10^{-3}	[42]
Second dendritic arm spacing	λ_2	m	0.65×10^{-4}	1.85×10^{-4}	[42]
Diffusion coefficient (liquid)	D_{ℓ}	m^{2} s^{-1}	4.5×10^{-9}	4.5×10^{-9}	[43]
Initial temperature	$T_0 = T_{\mathrm{liq}}$	K	492.14	558.64	[42]
Heat transfer coefficient	h	W m^{-2} K^{-1}	400	400	[42]
External temperature	T_{EXT}	K	298	298	[42]
Density difference of solid and liquid	$\Delta\rho$	kg m^{-3}	304	420	[44]
Gibbs Thomson coefficient	Γ	m K	6.5×10^{-8}	7.9×10^{-8}	[45]
Initial inoculant number density	n_{em}	m^{-3} s^{-1}	1.0×10^{10}	1.0×10^{10}	
Initial equiaxed number density	n_{eq}	m^{-3} s^{-1}	1.0×10^{7}	1.0×10^{7}	
Gaussian distribution width	ΔT_N	K	3.0	3.0	
Undercooling for maximum grain production rate	ΔT_{σ}	K	5.0	5.0	

a numerical benchmark as suggested by Bellet et al. [42]. Only half of the test casting is calculated by setting a symmetry plane at the left boundary. Two different alloys are considered: one is Sn-10 wt%Pb with solute element Pb heavier than the solvent Sn; the other is Pb-18 wt%Sn with solute element Sn lighter than the solvent Pb. The solidified equiaxed crystal is considered always heavier than the melt. Thermodynamic data and thermal physical properties of both alloys are listed in Table 2. The casting is cooled unidirectionally, either from the bottom or from the top. Therefore, 4 test cases of calculations are defined and they are correspondent to 4 cases in the bottom row of Fig. 1.

3. Modeling results

3.1. Case E1

Case E1 (Fig. 1(e)) considers the solidification of Sn-10 wt%Pb alloy from the bottom. Both thermal and solutal buoyancy forces of the melt act downwards, but the buoyancy force of the equiaxed phase, pointing downwards as well, is dominant over the thermal and solutal buoyancy forces of the melt. The solidification sequence is shown in Fig. 3.

Nucleation of equiaxed crystals and solidification start from the bottom wall, gradually extend to the upper region. The inoculants, as quantified by their number density n_{em} (Fig. 3(c.x) in color scale), begins to be activated as and transferred into equiaxed nuclei, which can grow as equiaxed grains. The number density of equiaxed grains n_{eq} is also shown in the same figure Fig. 3(c.x), but as isolines. The equiaxed phase has higher density than the melt; they tend to sink. Because the downward buoyancy force of the equiaxed phase overwhelms the thermal and solutal buoyancy forces of the melt. As shown in Fig. 3(b.x), the motion of equiaxed grains is mostly downwards. The velocity field of the melt (Fig. 3(a.x)) becomes very unstable. The sinking grains tend to drag the melt downwards on the one hand; sedimentation of equiaxed grains pushes the melt upwards on the other hand. During the early stage of solidification (Fig. 3(a.2)), some vortexes of

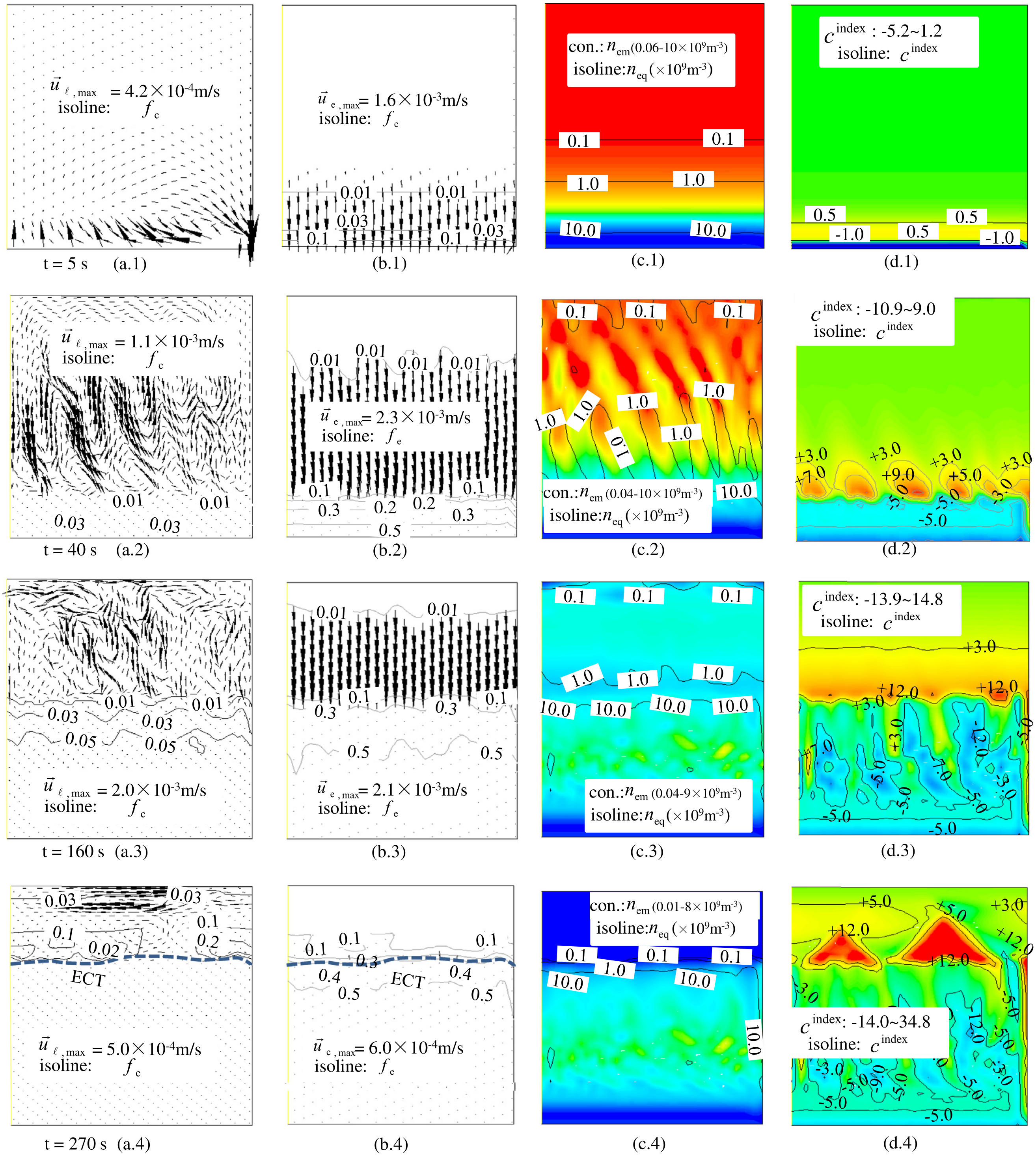

Fig. 3. Solidification sequence of Case E1. The column a.x shows the liquid velocity overlaid by f_c isolines, as well as the ECT (blue dash line in a.4); b.x shows the equiaxed velocity field overlaid by f_e isolines; c.x shows the evolution of n_{em} in color scale overlaid by n_{eq} isolines; d.x shows the evolution of macrosegregation index overlaid by its isolines. The alloy is Sn-10 wt%Pb. (For interpretation of the references to color in this figure legend, the reader is referred to the web version of this article.)

melt flow develop. With the progress of solidification, some vortexes merge together to form a few larger vortexes (Fig. 3(a.3)). Finally, a double diffusive convection cell is observed during the late stage of solidification (Fig. 3(a.4)).

The transport of n_{em} follows the melt flow, while the transport of n_{eq} follows the velocity of equiaxed phase. The sinking/sedimentation of equiaxed phase leads to the increase of both f_e (Fig. 3(b.x)) and n_{eq} (Fig. 3(c.x)) in the bottom region. The region of liquid-solid two phase mixture extends gradually to the upper part of the casting due to the continuous solidification and enhanced mixing by the crystal movement and melt flow. Nucleation event continues in the upper boarder of the two phase mixture region. During the late stage of solidification, almost all inoculants are consumed (Fig. 3(c.4)), and no further nucleation of equiaxed grains occurs. The remaining melt in the upper part of the casting can only solidify as columnar structure. The consumption of the inoculants stimulates the equiaxed-to-columnar transition (ECT).

The pile-up of equiaxed phase in the bottom region is shown in Fig. 3(b.x). As the amount of equiaxed phase increases to a certain limit at the bottom, i.e. f_e^{Env} $(=f_e/f_{si}) \geqslant f_{e,\mathrm{packing}}$, the motion of the equiaxed phase stops. The equiaxed grains can continue to grow, but they are stationary. The stationary equiaxed phase region can develop into a columnar structure, if no sufficient equiaxed phase (competing with the growth of columnar structure) exists in the columnar tip front. However, during the early stage of solidification (Fig. 3(a.1–3) and (b.1–3)), due to the continuous nucleation and growth of the equiaxed grains ahead of the columnar tip front no visible columnar structure (less than 0.03 of the maximum f_c) can be seen. The solidification structure is dominantly equiaxed. The ECT event occurs at ca. 243 s, when most inoculants are consumed in the upper region and no sufficient equiaxed grains exist in front of columnar tip front. The ECT boarder is observed in Fig. 3 (a.4). Below the ECT line it is dominant by equiaxed structure, while above the ECT line there is only columnar structure.

Fig. 3(d.x) shows the formation of macrosegregation. During the early stage of solidification (before ECT) the macrosegregation is caused by the crystal sedimentation. The accumulation of equiaxed phase at the bottom region induces the negative segregation. The solute-enriched melt is pushed upwards, leading to formation of a layer of positively segregated melt in the front of the two-phase mixture region. This positive segregation layer is not uniform (Fig. 3(d.2)), because of the vortexes of the melt flow. This positive segregation layer is also not stable, because the subsequent solidification, crystal sedimentation and melt flow will adapt its distribution. With the progress of solidification, some weak positively-segregated bands form (Fig. 3(d.3)) in the packed equiaxed region. These weak positive segregation bands follow the traces of the quasi-steady vortexes in the melt flow. After ECT, the solidification structure is purely columnar, and the dominant mechanism of macrosegregation is the thermo-solutal convection. As we mentioned previously, both thermal and solutal buoyancy forces of the melt act downwards. The thermal and solutal buoyancy forces try to stabilize the melt, i.e. to minimize the flow. Therefore, the flow intensity at the late stage of solidification becomes very weak ($\sim 10^{-4}$ m/s), and the flow pattern is also adapted into a kind of double diffusive convection cell. Finally, two positively segregation regions are 'frozen' into the columnar structure just above the ECT line.

3.2. Case E2

Case E2 (Fig. 1(e)) considers the solidification of the alloy Pb-18 wt%Sn from the bottom. The settings of this case are the same as the Case E1 except for the alloy. In Case E2 the solute element (Sn) is now lighter than the solvent (Pb), i.e. the solutal buoyancy force of the melt points upwards, leading to much stronger solutal convection ($\sim 10^{-2}$ m/s) than for the Case E1. The solidification sequence is shown in Fig. 4.

Initially, nucleation and solidification start from the bottom. Inoculants (n_{em}) begin to be activated as equiaxed nuclei (n_{eq}), Fig. 4(c.x). The equiaxed grains tend to sink (Fig. 4(b.x)), while the melt rises. The velocity field of the melt (Fig. 4(a.x)) is also unstable (similar to E1), but the flow pattern looks quite different from that of E1. Less number of vortexes and larger magnitude of the melt velocity are found for the current Case E2. The velocity field of the equiaxed phase is more chaotic.

The crystal sedimentation leads to pile-up of equiaxed crystals in the bottom. The region of the liquid-solid two phase mixture extends gradually towards the upper region. Nucleation of new equiaxed crystals continues at the upper border of the two phase mixture region. During the late stage of solidification, inoculants are almost consumed (Fig. 4(c.4)). The ECT event occurs at around 110 s. The remaining melt in the upper part solidifies as columnar structure.

Fig. 4(d.x) shows the formation of macrosegregation. During the early stage of solidification (before ECT) sedimentation-induced negative segregation is observed at the bottom. The solute-enriched melt is pushed upwards, leading to a gradual enrichment of solute in the bulk melt (similar to Case E1). The significant differences between cases E2 and E1 are the flow patterns and their magnitudes of melt flow. The large velocity of the melt for the Case E2 due to solutal convection enhances the solute mixing in the bulk melt, rather than the concentrated positively-segregated band in front of the liquid-solid two phase mixture region of Case E1. After ECT (110 s) the solidification structure is pure columnar, and the dominant mechanism of macrosegregation is thermo-solutal convection. Again, the large velocity magnitude of the interdendritic and bulk melt leads to formation of a large positive segregation, which is concentrated in the top surface region of the test case (Section 4.1, Fig. 7). As what we learnt from the Case C2 of Part I (pure columnar solidification of Pb -18 wt% Sn from bottom) [4], two positive segregation channels develop along both side boundaries in the Case E2 during the late stage of columnar solidification.

3.3. Case E3

Case E3 (Fig. 1(g)) considers the solidification of the alloy Pb-18 wt%Sn from the top. The equiaxed grains, as nucleated from the top, will sink immediately downwards, while the melt, as enriched with solute element Sn, tries to stay in the top region. The solidification sequence of this case, as shown in Fig. 5, becomes more dynamic than the last two cases (E1 and E2).

Nucleation (Fig. 5(c.x)) and solidification start from the top surface. The sinking equiaxed grains (Fig. 5(b.x)) drag the surrounding melt with them, initializing a transient melt flow in the bulk (Fig. 5 (a.x)). This transient flow brings inoculants from lower region to upper cold region where nucleation continues. The sinking velocity of equiaxed phase is very large (~ 0.02 m/s), and the equiaxed phase piles up at the bottom. The further solidification process includes: (1) transport of inoculants by the melt flow to upper regions, where nucleation continues; (2) growth of equiaxed grains; (3) sinking of equiaxed grains and further pile-up of equiaxed phase at the bottom. An interesting phenomenon (Fig. 5(c.x)) is that the settling equiaxed crystals can entrap a part of rest melt in the inter-granular space. That means that a part of inoculants might also be entrapped there without being activated as equiaxed nuclei. In this case the ECT event occurs quite early, at around 70 s. The rest melt in the upper region solidifies as columnar structure.

Fig. 5(d.x) shows the formation of macrosegregation. In principle, the macrosegregation mechanism of equiaxed solidification (before ECT) is similar to the last two cases as cooled from the bottom, E1 and E2. The main difference is that the solute mixing is more effective for Case E3. Generally, one can see a similar segregation pattern as that of E1 and E2: i.e. sedimentation-induced negative segregation at the bottom region and a positive segregation in the top, but the transition zone from negative to positive segregation is wider. After ECT melt flow during columnar solidification adapts the distribution in the upper region. At the end of solidification a relatively strong positive segregation at the top surface region is observed.

3.4. Case E4

Case E4 (Fig. 1(h)) considers solidification of alloy Sn-10 wt%Pb from the top. The solidification sequence is shown in Fig. 6. Solidification of this case is quite similar to Case E3, especially

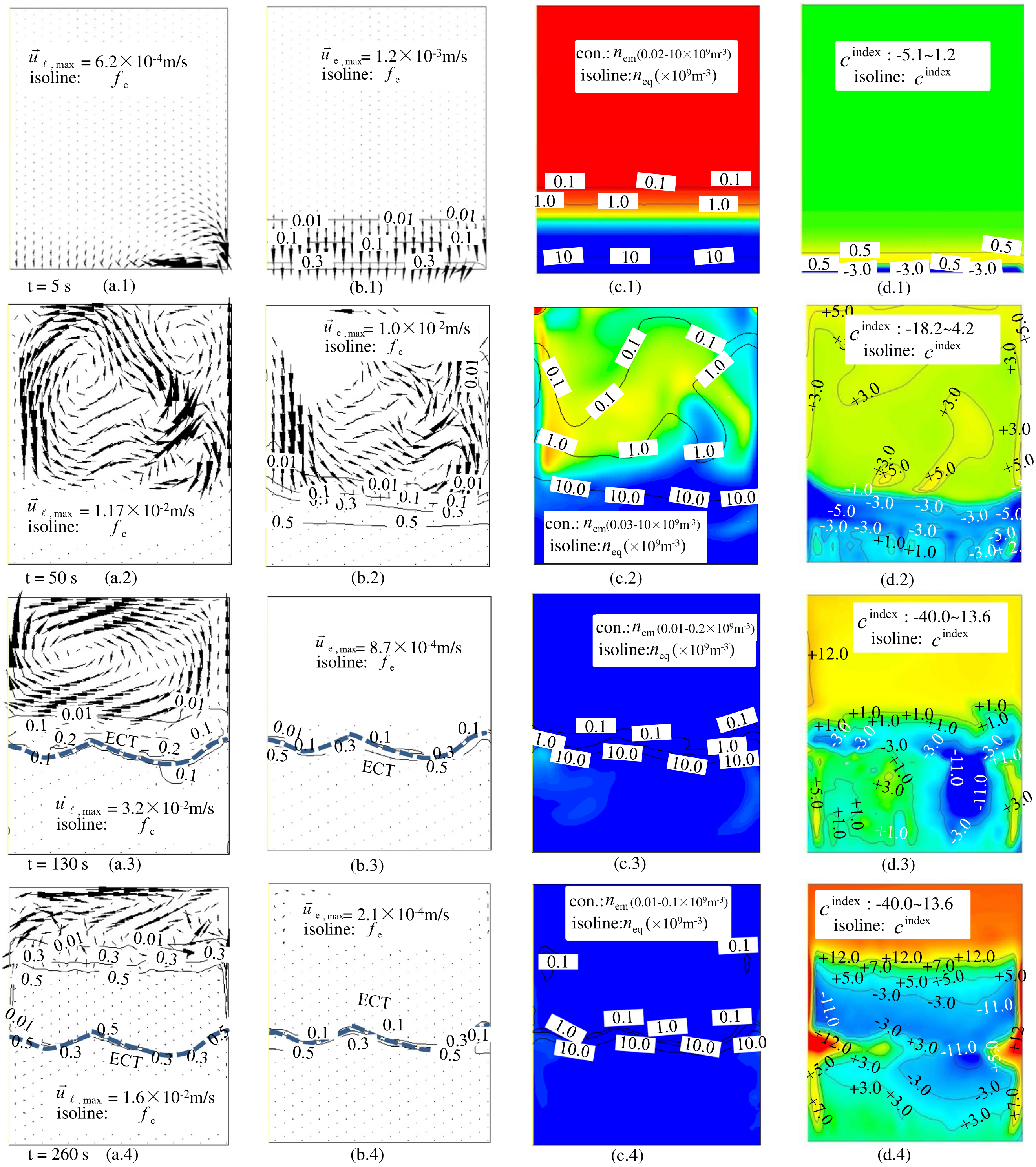

Fig. 4. Solidification sequence of Case E2. The column a.x shows the liquid velocity overlaid by f_c isolines, as well as the ECT (blue dash line in a.3, a.4); b.x shows the equiaxed velocity field overlaid by f_e isolines; c.x shows the evolution of n_{em} in color scale overlaid by n_{eq} isolines; d.x shows the evolution of macrosegregation index overlaid by its isolines. The considered alloy is Pb-18 wt%Sn. (For interpretation of the references to color in this figure legend, the reader is referred to the web version of this article.)

during the early stage. Analysis of the early stage equiaxed solidification can refer to that of Case E3. The major difference between this Case E4 and the Case E3 is the late stage of columnar solidification. ECT occurs at 125 s. After ECT the columnar primary tip front grows very fast, and the columnar structure spreads from the ECT line immediately into the entire upper region, leaving the remaining melt solidifying in the large inter-columnar region (mushy zone). As the casting is cooled continuously from the top surface, the upper surface is in favor of solidification. The upper surface solidifies faster than the inner region of the mushy zone. The thermo-solutal convection is still quite active in the mushy zone. The solutal buoyancy force of this alloy points downwards, in the same direction of the thermal buoyancy force. The last-to-solidify region of the Case E4 is located in the region close to ECT line. Therefore, the large area of positive segregation in the upper region, which has formed during the early stage equiaxed

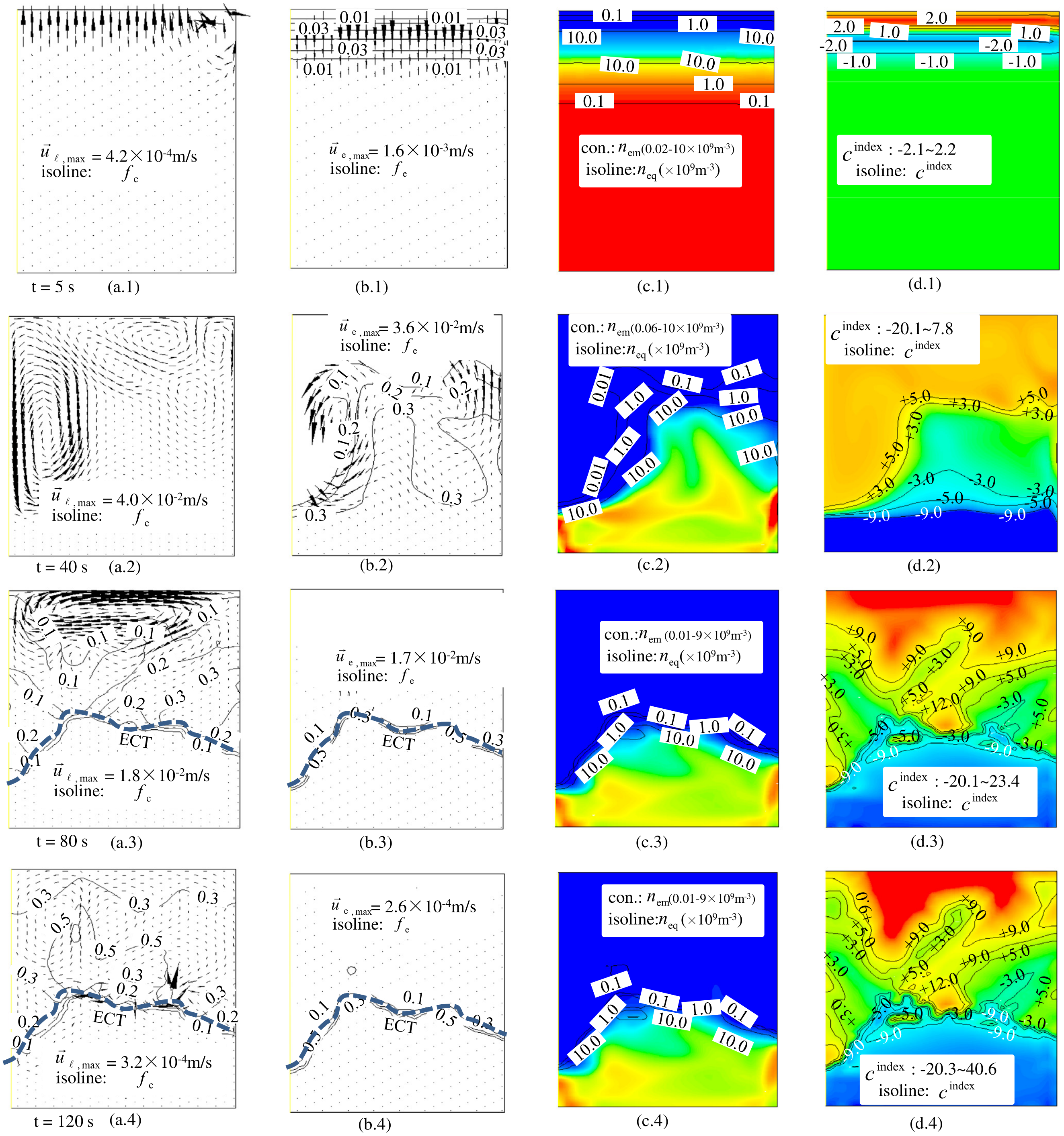

Fig. 5. Solidification sequence of Case E3. The column a.x shows the liquid velocity overlaid by f_c isolines, as well as the ECT (blue dash line in a.3, a.4); b.x shows the equiaxed velocity field overlaid by f_e isolines; c.x shows the evolution of n_{em} in color scale overlaid by n_{eq} isolines; d.x shows the evolution of macrosegregation index overlaid by its isolines. The considered alloy is Pb-18 wt%Sn. (For interpretation of the references to color in this figure legend, the reader is referred to the web version of this article.)

solidification, is gradually driven into the last-to-solidify region by the thermo-solutal convection. This leads to the formation of a large positive segregation band above the ECT line.

4. Discussion

4.1. Macrosegregation intensity by different mechanisms

The calculated macrosegregation results of the 4 test cases of equiaxed solidification are compared in Fig. 7. The segregation distribution is shown in color scale, but its intensity is analyzed by the c^{index} distribution range as labeled in the figures and by the global macrosegregation intensity (GMI). GMI is used to evaluate the global average segregation intensity, while the c^{index} distribution range is used to quantify the macrosegregation extremes.

During equiaxed solidification, there are four mechanisms which lead to the formation of macrosegregation: crystal sedimentation, thermal buoyancy flow, solutal buoyancy flow and species diffusion in the interdendritic/inter-granular melt. We learnt from Part I [4] that the diffusion-induced surface segregation falls into

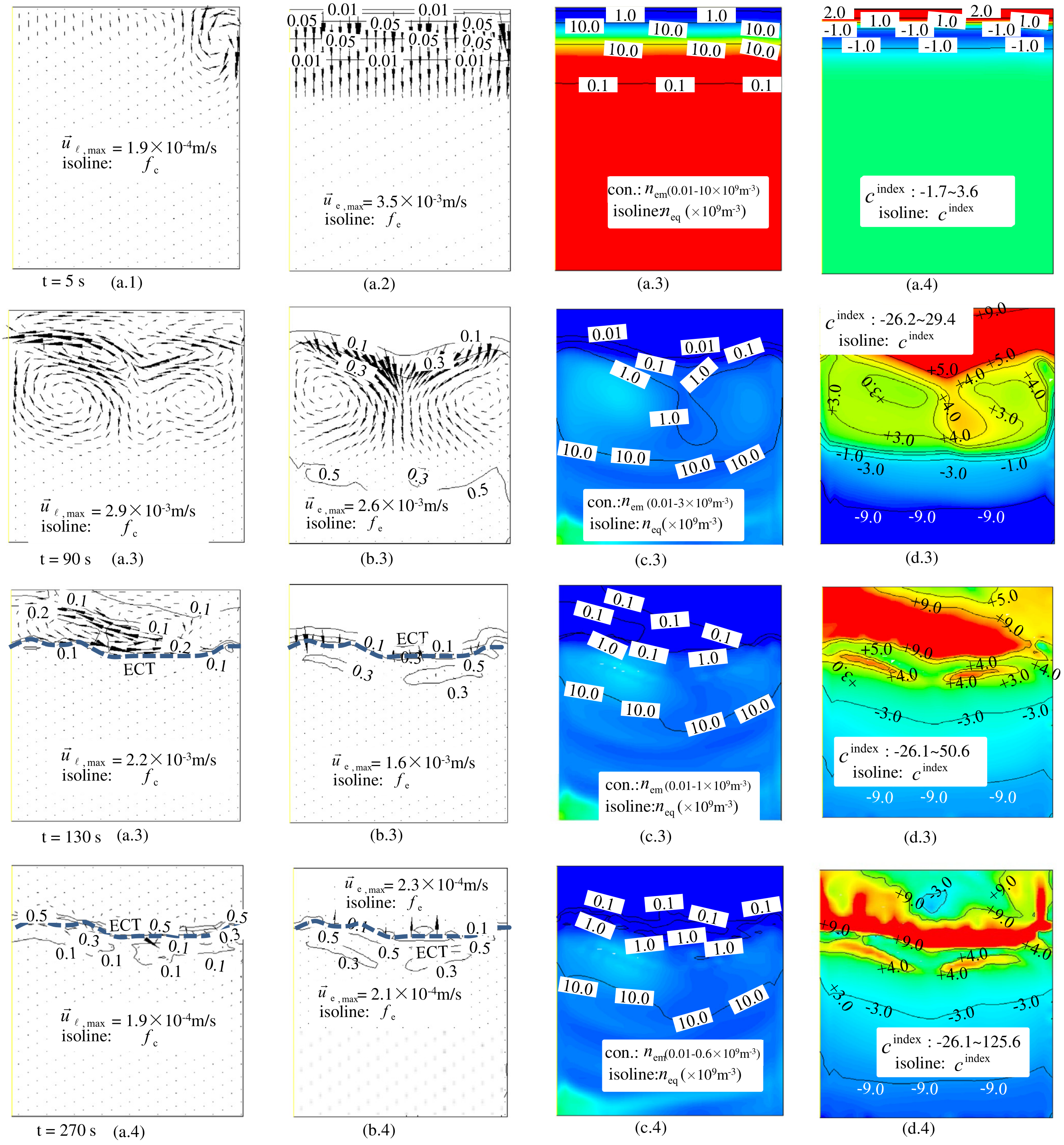

Fig. 6. Solidification sequence of Case E4. The column a.x shows the liquid velocity overlaid by f_c isolines, as well as the ECT (blue dash line in a.3, a.4); b.x shows the equiaxed velocity field overlaid by f_e isolines; c.x shows the evolution of n_{em} in color scale overlaid by n_{eq} isolines; d.x shows the evolution of macrosegregation index overlaid by its isolines. The considered alloy is Sn-10 wt%Pb. (For interpretation of the references to color in this figure legend, the reader is referred to the web version of this article.)

the range of $|c^{index}| < 4\%$ or GMI < 0.1. Thus, it is ignorable in comparison to the sedimentation-induced segregation (Fig. 7). Among the other three mechanisms, crystal sedimentation is dominant. Evidently, during early stage of solidification, a negative segregation zone develops at the bottom, and the bulk melt in the upper region is gradually enriched with solute (Figs. 3–6). No matter what alloy is considered and which cooling condition (cooling from top or from bottom) is applied, settling of equiaxed crystals at the bottom leads to negative segregation. Further theoretical analysis of the sedimentation-induced macrosegregation is carried out in Section 4.2. The intensity/strength of sedimentation-induced negative segregation at the bottom region is in the order of $c^{index} = -10\%$. For some special cases, c^{index} might reach extreme value of -32% at certain position. After ECT, only two flow mechanisms operate: thermal and solutal buoyancy. The concentration distribution in the upper region is then adapted by the thermo-solutal convection during columnar solidification. As mentioned above, the remaining melt in the upper part after ECT is normally enriched with solute, i.e. positively-segregated. The formation of the final positive segregation distribution depends on the alloy and cooling direction [4]. Therefore, different positive segregation patterns are observed for the cases, E1–E4.

Can one estimate the macrosegregation tendency based on the simple settings of each case (E1–E4) without performing any simulation? The answer is: difficult to estimate. Although we know that the start of equiaxed solidification leads to a negative segregation at the bottom, the occurrence of ECT and the final distribution of positive segregation in the upper region during columnar solidification governed by thermo-solutal convection cannot be estimated. If no ECT occurs, things become easier. With the ECT, the dominant macrosegregation mechanism is changed from crystal sedimentation to thermo-solutal convection. Furthermore, the macrosegregation as induced by thermo-solutal buoyancy depends on the alloy and cooling direction.

Can a technical alloy solidify as pure equiaxed structure without ECT? According to the classical heterogeneous nucleation theory, equiaxed nuclei originate from exogenous particles/inoculants which exist in the parent melt. The nucleation event creates new crystals, and in the meantime it consumes the inoculants. If all inoculants are consumed and the equiaxed crystals are transported away, the remaining melt has to solidify as columnar structure. We assume that no other nucleation mechanism operates, e.g., homogenous nucleation, crystal multiplication, or fragmentation of columnar dendrites. The modeling results of Fig. 7 show ECT for all cases. It implies the difficulty to get pure equiaxed structure in technical alloys by gravity casting techniques.

Notice that the assumed symmetry boundary condition for the left side of the test casting influences the calculation accuracy of macrosegregation. This symmetry boundary corresponds to an adiabatic and free-slip boundary, and no mass is allowed to cross the boundary. The reality might be different. Therefore, for engineering application of the macrosegregation model, special caution must be taken for the assumption of symmetry.

From the study of pure columnar solidification in Part 1 [4], we knew that the macrosegregation intensity is related to the velocity magnitude of flow. We anticipate that this relationship should apply for equiaxed solidification as well. The modeling results of Fig. 7, however, do not clearly show this relationship. The reason is that for all 4 test cases of equiaxed solidification, the velocity magnitude of crystal sedimentation and flow are in the similar range, i.e. 10^{-3}–10^{-2} m/s. The labeled maximum velocity in Fig. 7 is the value at a certain moment and at a certain position, it does not represent statistic average velocity magnitude during the solidification process. Generally, during equiaxed solidification the velocity magnitude of the crystal sedimentation and the flow is larger than that of thermo-solutal convection during pure columnar solidification. The difference of macrosegregation intensity among all 4 equiaxed solidification cases is not so large, and they are in the similar range, i.e. c^{index} from −25 to +180%, and GMI is from 5 to 33.

Another interesting phenomenon as observed is that the final area of equiaxed zone of test cases E1 and E4 (alloy Sn–10 wt% Pb) is evidently larger than that of test cases E2 and E3 (alloy Pb–18 wt%Sn). The modeling result (Fig. 7) implies that the final area of equiaxed zone is mostly dependent on the alloy rather than the cooling (solidification) direction. As the total number of nucleation inoculants are set equal for all test cases and most inoculants are eventually activated as equiaxed nuclei, the smaller area of equiaxed zone (E2 and E3) corresponds to the finer equiaxed grains. This kind of alloy-dependency of the equiaxed zone (or grain size) can be explained by the so-called "growth-restricting effect" GRE according to Hellawell and Maxwell [46,47], where $GRE = m(k-1)c_0$. The role of solute element in an alloy is to restrict the growth rate of the growing interface, which, in turn,

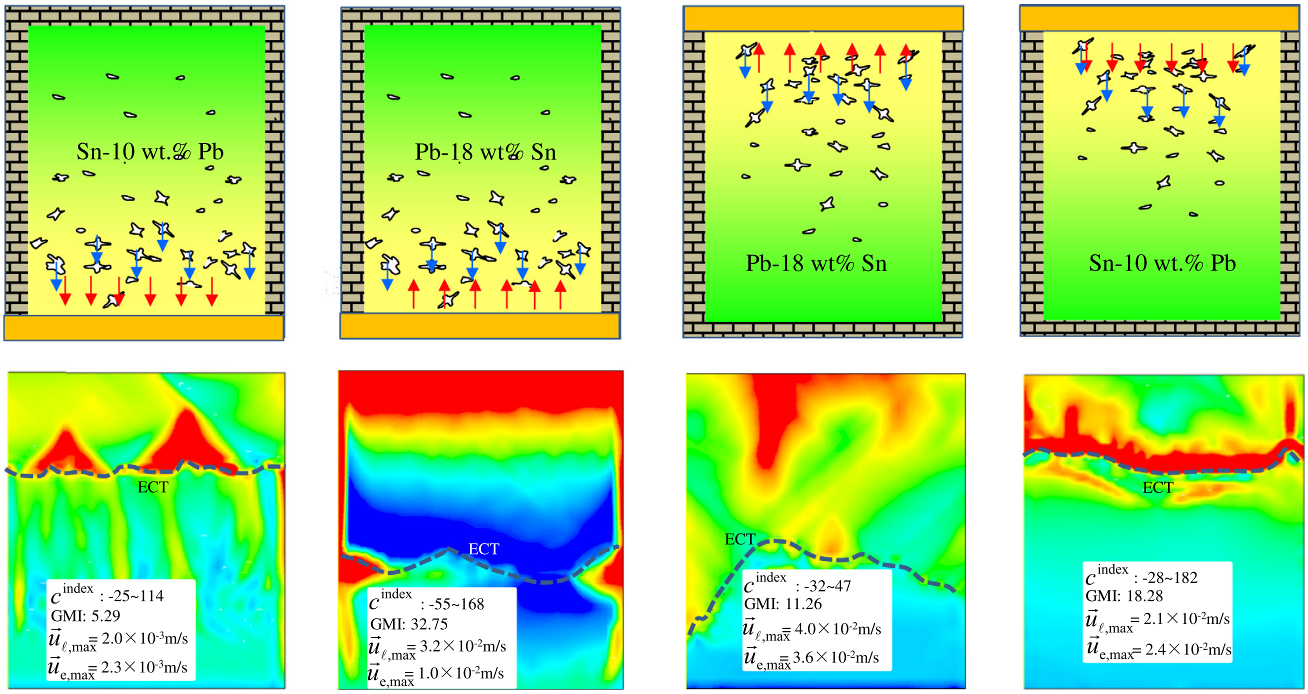

(a) Case E1 (b) Case E2 (c) Case E3 (d) Case E4

Fig. 7. Comparison of the final macrosegregation patterns for the 4 test cases of equiaxed solidification. The segregation (c^{index} in %) contours are shown in color scale, and they have different distribution ranges, as labeled in the figure. The maximum flow velocity and crystal sedimentation velocity during solidification and the global macrosegregation intensity (GMI) are also given. The yellow walls indicate chilled walls, while the hatched ones are adiabatic. (For interpretation of the references to color in this figure legend, the reader is referred to the web version of this article.)

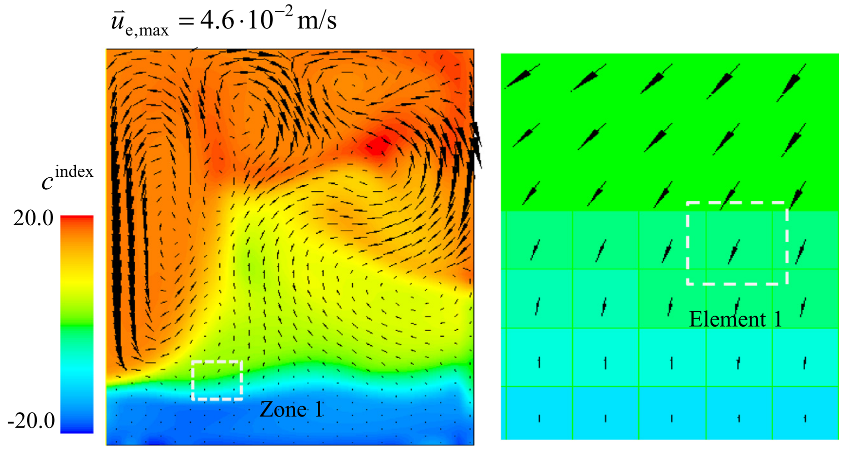

(a) (b)

Fig. 8. Solidification event in Case E3 ($t = 30$ s): Pb-18 wt%Sn cooling from the top. (a) Macrosegregation index overlaid by equiaxed velocity vectors; (b) zoom-in view of Zone 1.

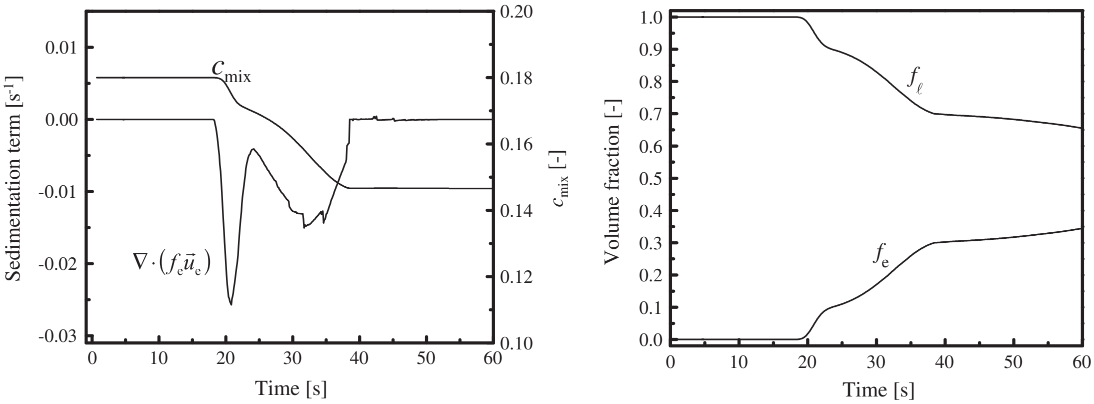

(a) (b)

Fig. 9. Analysis of c_{mix} evolution of in a reference element (element 1 as marked in Fig. 8(b)). (a) Sedimentation term and mixture concentration; (b) volume fractions of phases.

allows more time for further nucleation events to occur. Therefore, a large value of GRE can be related to a fine equiaxed structure, i.e. small area of equiaxed zone. The GRE values for alloy Sn–10 wt%Pb and Pb–18 wt%Sn are 12 and 29 correspondingly.

4.2. Sedimentation-induced macrosegregation

Sedimentation-induced macrosegregation during equiaxed solidification can be analyzed according to the transport of equiaxed phase, which is described by the following equation [21]:

$$\frac{\partial}{\partial t}(c_{\mathrm{mix}}) \approx (c_\ell - c_{\mathrm{e}}) \cdot \nabla \cdot \left(f_{\mathrm{e}} \vec{u}_{\mathrm{e}}\right) \tag{28}$$

Variation of the local mixture concentration, c_{mix}, depends on the concentration difference between the melt and the equiaxed phase, $c_\ell - c_{\mathrm{e}}$, and the divergence of the superficial velocity of the equiaxed phase, $\nabla \cdot (f_{\mathrm{e}} \vec{u}_{\mathrm{e}})$, which is also named as sedimentation term. $c_\ell - c_{\mathrm{e}}$ is always positive for alloys with partitioning coefficient k less than one. The sedimentation term, $\nabla \cdot (f_{\mathrm{e}} \vec{u}_{\mathrm{e}})$, gives an indication about the local depletion or accumulation of equiaxed crystals. For example, a negative value of $\nabla \cdot (f_{\mathrm{e}} \vec{u}_{\mathrm{e}})$ means accumulation of equiaxed crystals in the local volume element. According to Eq. (28), the accumulation of equiaxed crystals would lead to a negative value of $\partial c_{\mathrm{mix}}/\partial t$, i.e. the decrease of c_{mix}, and thus to the formation of negative segregation.

Eq. (28) can be applied to analyze the sedimentation-induced macrosegregation of the current benchmark. An example is shown in Figs. 8 and 9. In Zone 1 of Fig. 8, the equiaxed velocity slows down and equiaxed crystals settle. Taking one reference element (Element 1) in Zone 1, the evolution of quantities of c_{mix}, $\nabla \cdot (f_{\mathrm{e}} \vec{u}_{\mathrm{e}})$, f_{e} and f_ℓ are tracked. Between 23 and 50 s a strong negative sedimentation term $\nabla \cdot (f_{\mathrm{e}} \vec{u}_{\mathrm{e}})$ occurs, and f_{e} increases correspondingly. As consequence c_{mix} decreases and a negative segregation appears there.

Similar to the study in Part 1 [4], thermo-solutal convection induced macrosegregation during columnar solidification after ECT can be analyzed according to the flow-solidification interaction [21].

4.3. Mesh sensitivity

Calculations with 8 different mesh (grid) sizes for the Case E3 were performed, and the resulting segregation patterns are shown in Fig. 10. As the mesh size decreases from 2.0 mm to 0.8 mm, the global segregation tendencies are quite similar: a positive

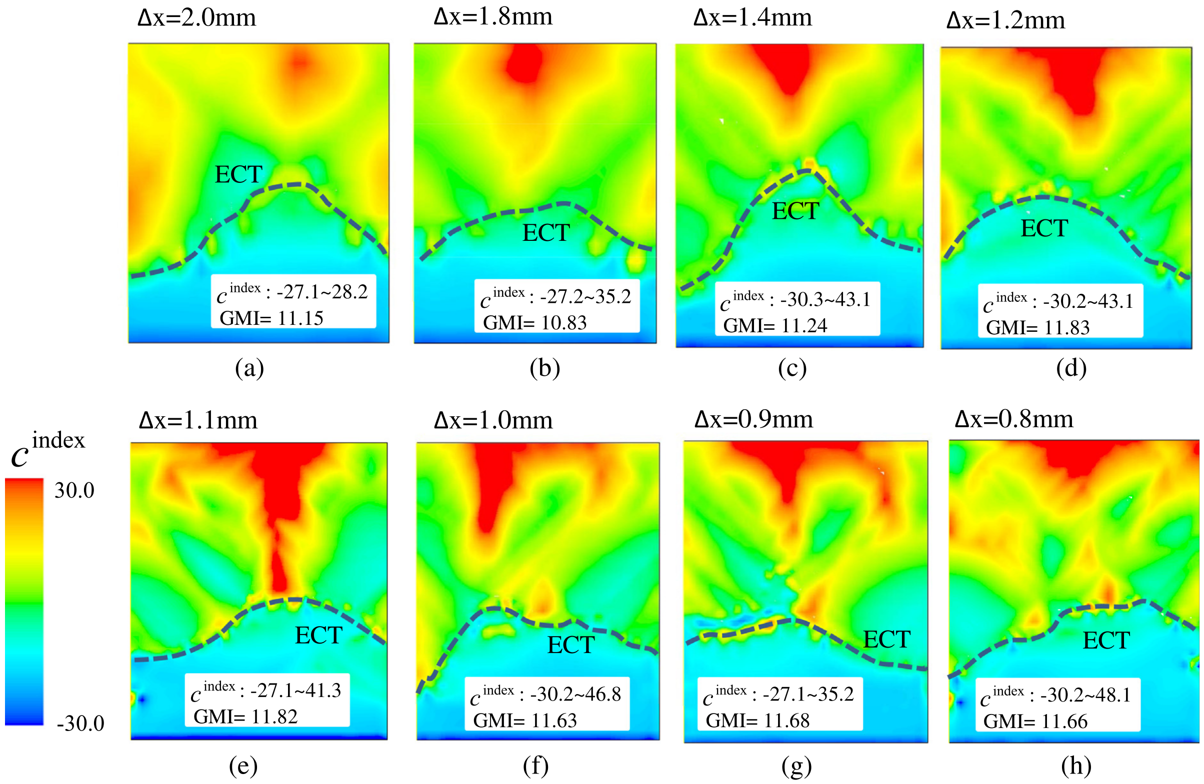

Fig. 10. Mesh sensitivity of macrosegregation predictions for Case E3. The macrosegregation contours are shown in color scale for mesh sizes of (a) 2.0 mm, (b) 1.8 mm, (c) 1.4 mm, (d) 1.2 mm, (e) 1.1 mm, (f) 1.0 mm, (g) 0.9 mm and (h) 0.8 mm.

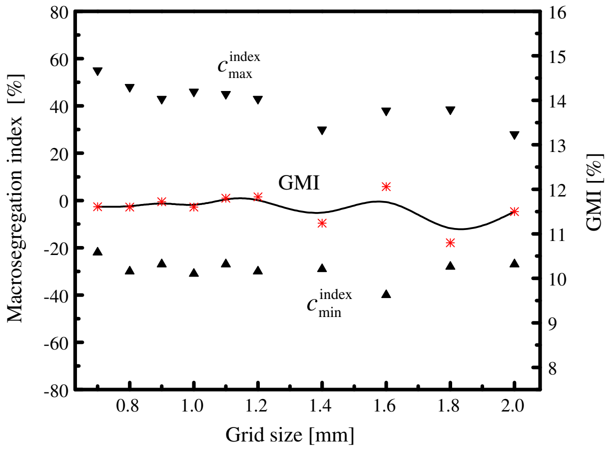

Fig. 11. Influence of mesh size on the macrosegregation extremes and GMI (Case E3).

macrosegregation zone in the upper region, a crystal sedimentation induced negative segregation zone in the bottom region, and a negative-to-positive transition zone is observed near the ECT line. In order to perform the evaluation of the mesh sensitivity more precisely, the c^{index} distribution range (segregation extremes $c^{\mathrm{index}}_{\mathrm{min}}$, $c^{\mathrm{index}}_{\mathrm{max}}$) and the global macrosegregation intensity (GMI) are plotted in Fig. 11 against the mesh (grid) size. The variation of GMI with different mesh sizes is quite small. As the mesh size is reduced to 1.2 mm, GMI seems to become stable at a value of 11.7. That means that a relative coarse mesh (1.2 mm) is sufficient for the prediction of the global macrosegregation intensity.

The distribution of c^{index} varies with the mesh size, even when the mesh size is reduced to as small as 0.8 mm (Fig. 10). The area of equiaxed zone (the negative segregation zone below the ECT line) seems to be similar for all calculations with different mesh sizes, but the shapes of the ECT line are different. The most significant difference between those calculations of different mesh sizes is the distribution of positive segregation in the upper pure columnar solidification region. Although a large positive segregation zone which mostly concentrates near the top surface is predicted by all calculations, the details of its distribution are different. The quantitative analysis of the segregation extremes ($c^{\mathrm{index}}_{\mathrm{min}}$, $c^{\mathrm{index}}_{\mathrm{max}}$) in Fig. 11 shows that no converged results are obtained, even when the mesh size is reduced to 0.8 mm. This kind of mesh dependency is understandable. In the early stage of equiaxed solidification, the details of crystal sedimentation and the induced melt flow are slightly mesh-dependent; hence the ECT line is also slightly influenced by the mesh size. In the late stage of columnar solidification, the interdendritic flow is also slightly mesh-dependent; hence the final distribution of the positive segregation is influenced by the mesh size. However, key features of the predicted global segregation patterns of different test cases are valid. The modeling results presented in this paper are based on the mesh size of 1 mm.

5. Conclusions

In order to provide exercise examples for metallurgical students to learn different macrosegregation mechanisms, a simple 2D casting with ideal configuration of equiaxed solidification was simulated by using a volume-average based solidification model [3]. The model was modified by (i) consideration of heterogeneous nucleation of equiaxed crystals and transport of inoculants and (ii) consideration of equiaxed-to-columnar transition (ECT). 4 test cases were calculated where cooling occur unidirectionally, either upwards or downwards. It was believed that the final macrosegregation tendency in each test case should be estimated without performing any simulation. However, the modeling results show that more complicated details of macrosegregation distribution can develop due to the complexity of the equiaxed-to-columnar transition (ECT). Following conclusions were drawn.

(1) Even for such simple case of equiaxed solidification, it is quite difficult to estimate the final macrosegregation tendency without performing any simulation. The main difficulty arises from the ECT. During the early stage of equiaxed solidification before ECT, the macrosegregation tendency is predictable: equiaxed sedimentation, i.e. the dominant macrosegregation mechanism, induces negative segregation in the bottom region; while solute-enriched melt is distributed in the upper region. After the ECT during the late stage of columnar solidification, the thermo-solutal convection becomes the dominant macrosegregation formation mechanism. The redistribution of the positive macrosegregation pattern in the upper region by thermo-solutal convection depends on the alloy and cooling direction.

(2) According to the classical heterogeneous nucleation theory [35,40] that equiaxed nuclei originate from exogenous particles/inoculants, it is difficult to get pure equiaxed structure in technical alloys by gravity casting technique. The modeling results show that an ECT event occurs during late stage of solidification when all inoculants are consumed. The remaining melt in the upper part of the test casting solidifies as columnar structure.

(3) Although we found that the macrosegregation intensity during pure columnar solidification increased with the velocity magnitude of melt flow, the modeling results did not clearly show this relationship in the 4 test cases of equiaxed solidification.

Calculation of macrosegregation is sensitive to the mesh size. The fine details of the c^{index} distribution should be interpreted with caution regarding mesh quality, but key features of the predicted segregation patterns of the 4 test cases of equiaxed solidification are valid.

Other 4 cases of pure columnar solidification were presented as Part I in a previous paper [4].

Acknowledgements

The authors acknowledge the financial support from Austrian Research Promotion Agency (FFG) through the project of Bridge Early Stage (No. 842441), as well as the technical support from the industrial partner Primetals Technologies (former Siemens VAI).

References

[1] J.A. Dantzig, M. Rappaz, Solidification, EPFL Press, 2009.
[2] A. Ludwig, Lecture note on solidification course in Swiss Federal Institute of Technology of Lausanne (EPFL), Lausanne, 2015.
[3] M. Wu, A. Ludwig, Metall. Mater. Trans. A 37 (2006) 1613–1631.
[4] M. Wu, Y. Zheng, A. Kharicha, A. Ludwig, Comput. Mater. Sci. 124 (2016) 444–455.
[5] W. Kurz, D.J. Fisher, Fundamentals of Solidification, third ed., Trans Tech Pub, Aedermannsdorf, Switzerland, 1992.
[6] M.C. Flemings, Solidification Processing, McGraw-Hill, 1974.
[7] M.C. Flemings, ISIJ Int. 40 (2000) 833–841.
[8] A. Ohno, Solidification: The Separation Theory and Its Practical Applications, Springer Science & Business Media, 1987.
[9] J. Ni, C. Beckermann, Metall. Mater. Trans. B 22 (1991) 349–361.
[10] C. Beckermann, R. Viskanta, Appl. Mech. Rev. 46 (1993) 1–27.
[11] J. Ni, C. Beckermann, J. Mater. Process. Manuf. Sci. 2 (1993) 217–231.
[12] M. Wu, A. Ludwig, J. Luo, Mater. Sci. Forum. 475–479 (2005) 2725–2730.
[13] M. Wu, A. Ludwig, L. Ratke, Model. Simul. Mater. Sci. 11 (2003) 755–769.
[14] R. Nadella, D. Eskin, Q. Du, L. Katgerman, Prog. Mater. Sci. 53 (2008) 421–480.
[15] C. Wang, C. Beckermann, Metall. Mater. Trans. A 27 (1996) 2754–2764.
[16] M. Wu, A. Ludwig, Acta Mater. 57 (2009) 5621–5631.
[17] M. Wu, A. Ludwig, Acta Mater. 57 (2009) 5632–5644.
[18] A. Ciobanas, Y. Fautrelle, J. Phys. D: Appl. Phys. 40 (2007) 3733–3741.
[19] Ø. Nielsen, A. Mo, B. Appolaire, H. Combeau, Metall. Mater. Trans. A 32 (2001) 2049–2060.
[20] N. Leriche, H. Combeau, C.-A. Gandin, M. Založnik, IOP Conf. Ser.: Mater. Sci. Eng. 84 (2015) 012087.
[21] M. Wu, L. Konozsy, A. Ludwig, W. Schutzenhofer, R. Tanzer, Steel Res. Int. 79 (2008) 637–644.
[22] A. Ludwig, M. Gruber-Pretzler, F. Mayer, A. Ishmurzin, M. Wu, Mater. Sci. Eng. A 413 (2005) 485–489.
[23] M. Wu, J. Li, A. Ludwig, A. Kharicha, Comput. Mater. Sci. 79 (2013) 830–840.
[24] M. Wu, J. Li, A. Ludwig, A. Kharicha, Comput. Mater. Sci. 92 (2014) 267–285.
[25] M. Wu, A. Fjeld, A. Ludwig, Comput. Mater. Sci. 50 (2010) 32–42.
[26] M. Ahmadein, M. Wu, J. Li, P. Schumacher, A. Ludwig, Metall. Mater. Trans. A 44 (2013) 2895–2903.
[27] M. Ahmadein, M. Wu, A. Ludwig, J. Cryst. Growth 417 (2015) 65–74.
[28] B. Appolaire, V. Albert, H. Combeau, G. Lesoult, Acta Mater. 46 (1998) 5851–5862.
[29] A. Kharicha, M. Stefan-Kharicha, A. Ludwig, M. Wu, Metall. Mater. Trans. A 44 (2013) 650–660.
[30] A. Badillo, D. Ceynar, C. Beckermann, J. Cryst. Growth 309 (2007) 216–224.
[31] A. Badillo, D. Ceynar, C. Beckermann, J. Cryst. Growth 309 (2007) 197–215.
[32] C.A. Gandin, S. Mosbah, T. Volkmann, D.M. Herlach, Acta Mater. 56 (2008) 3023–3035.
[33] L. Hachani, K. Zaidat, Y. Fautrelle, Int. J. Heat Mass Transfer 85 (2015) 438–454.
[34] M. Wu, A. Ludwig, Metall. Mater. Trans. A 38A (2007) 1465–1475.
[35] M. Rappaz, Int. Mater. Rev. 34 (1989) 93–123.
[36] J. Li, M.H. Wu, A. Ludwig, A. Kharicha, P. Schumacher, Mater. Sci. Forum 790 (2014) 121–126.
[37] R.B. Bird, W.E. Stewart, E.N. Lightfoot, Transport Phenomena, Wiley, 2006.
[38] A. Ludwig, M. Wu, Metall. Mater. Trans. A 33 (2002) 3673–3683.
[39] J. Lipton, M.E. Glicksman, W. Kurz, Mater. Sci. Eng. 65 (1984) 57–63.
[40] T. Quested, A. Greer, Acta Mater. 52 (2004) 3859–3868.
[41] M. Bedel, K. Tveito, M. Založnik, H. Combeau, M. M'Hamdi, Comp. Mater. Sci. 102 (2015) 95–109.
[42] M. Bellet, H. Combeau, Y. Fautrelle, D. Gobin, M. Rady, E. Arquis, O. Budenkova, B. Dussoubs, Y. Duterrail, A. Kumar, Int. J. Therm. Sci. 48 (2009) 2013–2016.
[43] M. Klassen, J. Cahoon, Metall. Mater. Trans. A 31 (2000) 1343–1352.
[44] J. Gu, C. Beckermann, Metall. Mater. Trans. A 30 (1999) 1357–1366.
[45] E. Cadirli, M. Gündüz, J. Mater. Sci. 35 (2000) 3837–3848.
[46] I. Maxwell, A. Hellawell, Acta Metall. 23 (1975) 229–237.
[47] M. Easton, D. Stjohn, Metall. Mater. Trans. A 30 (1999) 1613–1623.